

Construction of Ag₂S@CaTiO₃ heterostructure photocatalysts for enhanced photocatalytic degradation of dyes

Yuxiang Yan^a, Hua Yang^{a,*}, Zao Yi^b, Tao Xian^c, Ruishan Li^a, Xiangxian Wang^a

^aState Key Laboratory of Advanced Processing and Recycling of Non-ferrous Metals, Lanzhou University of Technology, Lanzhou 730050, China, Tel. +86 931 2973783; Fax: +86 931 2976040; emails: hyang@lut.edu.cn (H. Yang), yanyx@lut.cn (Y.X. Yan), liruishan@lut.cn (R.S. Li), wangxx869@lut.edu.cn (X.X. Wang)

^bJoint Laboratory for Extreme Conditions Matter Properties, Southwest University of Science and Technology, Mianyang 621010, China, email: yizaomy@swust.edu.cn

^cCollege of Physics and Electronic Information Engineering, Qinghai Normal University, Xining 810008, China, email: xiantao1985@126.com

Received 18 April 2019; Accepted 24 July 2019

ABSTRACT

In this work, we have assembled Ag₂S carbon quantum dots (CQDs) onto CaTiO₃ nanocuboids (NCs), aimed at creating Ag₂S@CaTiO₃ composite photocatalysts with superior photocatalytic performances. Scanning/transmission electron microscopy observation confirms the uniform decoration of Ag₂S CQDs (7–17 nm) on the surface of CaTiO₃ NCs with size of 0.8–1.1 μm in length and 0.3–0.5 μm in width. Photoluminescence, photocurrent response and electrochemical impedance spectroscopy investigations reveal that the Ag₂S@CaTiO₃ composites manifest highly efficient separation of photoexcited electron/hole pairs. The photocatalytic degradation activity of the Ag₂S@CaTiO₃ composites was assessed by the removal of rhodamine B from aqueous solution. It is demonstrated that the composites exhibit photocatalytic degradation performance much superior to that of bare Ag₂S CQDs and CaTiO₃ NCs under ultraviolet irradiation. This can be explained as the result of efficient separation of photoexcited electron/hole pairs induced by the Z-scheme electron transfer. In addition, the composites also manifest enhanced visible-light photocatalytic performance when compared with bare CaTiO₃ NCs, implying that they can make the best use of the solar energy in the practical photocatalytic applications.

Keywords: CaTiO₃ nanocuboids; Ag₂S quantum dots; Ag₂S@CaTiO₃ composites; Photocatalytic degradation performance; Z-scheme electron transfer

1. Introduction

Water resources on which living beings, particularly human beings, depend are becoming seriously polluted due to the discharge of wastewater from chemical industries. The industrial wastewater contains large quantities of harmful and carcinogenic substances, such as organic dyes and pigments [1]. As most of the organic pollutants are hardly self-decomposed, their elimination by artificial management has become an imperative necessity. Semiconductor-based

photocatalysis, as a simple, low-cost and green technology, has shown tremendous application potential in the wastewater treatment [2–8]. It is particularly interesting that this technology is able to harness the power of the sun to degrade organic pollutants. The photocatalytic degradation reactions are highly correlated with photoexcited electrons (e⁻) in the conduction band (CB) and holes (h⁺) in the valence band (VB) of semiconductor photocatalysts. To make the semiconductor photocatalyst fully harness the solar spectrum and achieve an excellent photocatalytic performance, two of the

* Corresponding author.

key points have to be considered. One is that the photoexcited e^-/h^+ pairs must be efficiently separated, and thus more charge carriers are available for the photocatalytic reactions. The other is to enhance the visible-light absorption of photocatalysts. Nevertheless, most of important photocatalysts, particularly titanium-contained oxide semiconductors, can only absorb ultraviolet (UV) light to trigger their photocatalytic activity owing to their wide bandgap (~ 3.2 eV) [9–12]. To overcome the issues mentioned above, there have been developed various strategies to modify semiconductor photocatalysts [13–19].

Zero-/one-/two-dimensional nanostructured materials (e.g. metal nanoparticles, carbon quantum dots (CQDs), carbon nanotubes, graphene, Ag_2S CQDs) generally exhibit many interesting physicochemical characteristics, and they can be technologically applied in many fields, such as bio-imaging, energy conversion, optoelectronic devices, wave absorption, and sensors, and photocatalysis [20–31]. In the aspect of photocatalytic applications, these nanomaterials have been shown to be excellent modifiers or co-catalysts to improve the photocatalytic performances of semiconductor photocatalysts [32–38]. Among them, Ag_2S CQDs are particularly interesting because they can absorb a wide range of solar spectrum, from UV to near-infrared light. Besides their promising application as a visible-light-driven photocatalyst [39], Ag_2S CQDs have been widely integrated, as an ideal co-catalyst, with other semiconductors to form excellent composite photocatalysts [40–43]. Furthermore, the photo-corrosion of Ag_2S could be reduced by the construction of heterostructures.

Recently, a great deal of work has been concerned with the perovskite-type calcium titanate ($CaTiO_3$) due to its intriguing physical properties, such as phosphorescence, ferroelectricity, piezoelectricity, elasticity, and photocatalytic activity [44–47]. In particular, $CaTiO_3$ has been shown to be a promising photocatalyst for the photocatalytic decomposition of organic dyes [48–53]. Nevertheless, the practical application of $CaTiO_3$ for photocatalytic purification of wastewater is still limited due to its only response to UV irradiation and high recombination rate of photoexcited e^-/h^+ pairs. Various methods have been widely adopted to modify $CaTiO_3$ with the aim of improving its overall photo-activities, such as surface disorder engineering, noble metal decoration, impurity element doping and heterostructure construction [12,54–58]. Our recent work has shown that the morphology of $CaTiO_3$ also has an important effect on its photocatalytic activity; in particular, (010)/(101) facets exposed $CaTiO_3$ nanocuboids (NCs) manifest a higher photocatalytic activity than $CaTiO_3$ nanospheres [48]. In this work, we have developed a new type of $Ag_2S@CaTiO_3$ composite photocatalysts by decorating Ag_2S CQDs on the surface of $CaTiO_3$ NCs. Due to their staggered band structure configuration [48,59], Ag_2S and $CaTiO_3$ are expected to be coupled to form Z-scheme $Ag_2S/CaTiO_3$ heterostructures. The Z-scheme electron transfer process occurring in the composites not only promote the photoexcited e^-/h^+ pair separation, but also preserve the photoexcited electrons with high reduction capability in the CB of Ag_2S and holes with high oxidation capability in the VB of $CaTiO_3$. It is demonstrated that the as-prepared $Ag_2S@CaTiO_3$ composites exhibit a powerful degradation of rhodamine B

(RhB), and they could find the practical application for wastewater treatment.

2. Experimental

2.1. Preparation of $Ag_2S@CaTiO_3$ hybrid composites

$Ag_2S@CaTiO_3$ hybrid composites were prepared through a two-step method. The first step is to synthesize $CaTiO_3$ NCs by a hydrothermal route. Typically, 3.3 mmol (0.03663 g) of anhydrous calcium chloride ($CaCl_2$) was dissolved in 20 mL of deionized water to obtain solution A, 3 mmol (0.2396 g) of P25 was uniformly dispersed in 20 mL of deionized water to obtain suspension B, and 0.2 mol (8 g) of sodium hydroxide (NaOH) was dissolved in 40 mL of deionized water to form solution C. To the solution A was slowly added with the suspension B and then the solution C drop by drop. All the processes mentioned above were accompanied by a magnetic stirring. The obtained precursor mixture was loaded in a stainless steel autoclave with a 100 mL Teflon liner. The heat-treatment temperature was 200°C and time was 24 h. The product was collected and washed with deionized water and ethanol to remove the impurity ions. After 12 h of drying at 60°C, final $CaTiO_3$ NCs were obtained.

The second step is to assemble Ag_2S QDs on the surface of $CaTiO_3$ NCs. 0.5 g of the as-synthesized $CaTiO_3$ NCs was uniformly dispersed in 30 mL of deionized water with ultrasonic treatment for 30 min and magnetic stirring for another 30 min (designated as suspension D). A certain amount of $AgNO_3$ (0.0361, 0.0762, 0.121 and 0.1713 g) was added to the suspension D, followed by 1 h of magnetic stirring (designated as suspension E). A certain volume of 0.05 g mL⁻¹ Na_2S solution (0.51, 1.08, 1.71 and 2.42 mL) was added in 20 mL of deionized water, which was then slowly added to suspension E drop by drop. The obtained mixture was magnetically stirred for 5 h, during which Ag_2S QDs were assemble on the surfaced of $CaTiO_3$ NCs. To remove the impurity ions, the product was washed with deionized water and ethanol, following by 12 h of drying at 60°C. The product was obtained as $Ag_2S@CaTiO_3$ hybrid composite. The composite samples with different mass fractions of Ag_2S (5%, 10%, 15% and 20%) were obtained by adding different amounts of $AgNO_3$ and Na_2S , and they were correspondingly designated as 5% $Ag_2S@CaTiO_3$, 10% $Ag_2S@CaTiO_3$, 15% $Ag_2S@CaTiO_3$ and 20% $Ag_2S@CaTiO_3$.

2.2. Sample characterization methodologies

The phase purity and crystal structure of the samples were examined by means of X-ray powder diffraction (XRD) on a D8 Advance X-ray diffractometer ($\lambda_{Cu-K\alpha} = 0.15406$ nm). A JSM-6701F field-emission scanning electron microscope (SEM) was used to observe the morphology of the samples. A JEM-1200EX field-emission transmission electron microscope (TEM) equipped with energy-dispersive X-ray spectroscopy (EDS or EDX) was used to investigate the microstructure, chemical composition and elemental distribution of the samples. The element chemical states of the samples were determined by X-ray photoelectron spectroscopy (XPS) on a PHI-5702 multi-functional X-ray photoelectron spectrometer. To analyze the optical absorption and bandgap energy of the

samples, ultraviolet-visible diffuse reflectance spectroscopy (UV-vis DRS) measurement was performed on a TU-1901 double beam UV-vis spectrophotometer. Fourier-transform infrared (FTIR) analysis of the samples was performed on a spectrum two FTIR spectrophotometer. A RF-6000 fluorescence spectrophotometer ($\lambda_{\text{excitation}} = 375 \text{ nm}$) was employed to measure the photoluminescence (PL) spectra of the samples.

2.3. Photo-electrochemical measurement procedure

A CST 350 electrochemical workstation equipped with a three-electrode cell configuration was used to study the electrochemical impedance spectroscopy (EIS) and photocurrent response of the samples. In the three-electrode cell configuration, a standard calomel electrode (SCE) acted as the reference electrode and a platinum foil electrode served as the counter electrode. An electrode preparation procedure reported in the literature [60] used to prepare the working electrode. 15 mg of the samples, 0.75 mg of polyvinylidene fluoride (PVDF), 0.75 mg of carbon black and 1 mL of 1-methyl-2-pyrrolidione (NMP) were uniformly mixed together. The slurry mixture was dispersed uniformly on the surface of fluorine-doped tin oxide (FTO) thin film, and subjected to drying 60°C for 5 h. The effective area of the FTO thin film was $1 \times 1 \text{ cm}^2$. The used electrolyte was $0.1 \text{ mol L}^{-1} \text{ Na}_2\text{SO}_4$ aqueous solution. A 30 W low-pressure mercury lamp emitting UV light ($\lambda = 254 \text{ nm}$) was served as the light source. A 0.2 V bias voltage was used during the transient photocurrent measurement. A sinusoidal voltage pulse with amplitude of 5 mV was used for the EIS measurement (measured frequency range: 10^{-2} – 10^5 Hz).

2.4. Photocatalytic test procedure

The photocatalytic performances of the samples were assessed by removal of RhB in aqueous solution (5 mg L^{-1}). UV light emitted from a 30 W low-pressure mercury lamp ($\lambda = 254 \text{ nm}$, 0.09 W cm^{-2} at a distance of 1 cm) and visible light generated by a 200 W halogen-tungsten lamp ($\lambda > 400 \text{ nm}$, 0.52 W cm^{-2} at a distance of 1 cm) were separately used the light source. 100 mL of RhB and 0.1 g of the sample were loaded the photoreactor. The adsorption of RhB on the photocatalyst surface was examined by magnetic stirring the reaction solution in the dark for 30 min. During the photocatalytic degradation process, the RhB concentration was monitored by measuring the absorbance of the reaction solution at intervals of 30 min. To achieve this aim, 2.5 mL of the reaction solution was sampled from the photoreactor and the photocatalyst was removed by centrifugation. The absorbance of the reaction solution was measured using a UV-vis spectrophotometer at a given wavelength $\lambda_{\text{RhB}} = 554 \text{ nm}$. The degradation percentage of RhB ($D\%$) was determined according to $D\% = (C_0 - C_t)/C_0 \times 100\%$ (C_0 = initial RhB concentration; C_t = residual RhB concentration).

3. Results and discussion

Fig. 1. illustrates the XRD patterns of Ag_2S , CaTiO_3 and $15\%\text{Ag}_2\text{S}@/\text{CaTiO}_3$. For bare Ag_2S and CaTiO_3 , their diffraction peaks including positions and relative intensities can be perfectly indexed into the Ag_2S monoclinic structure

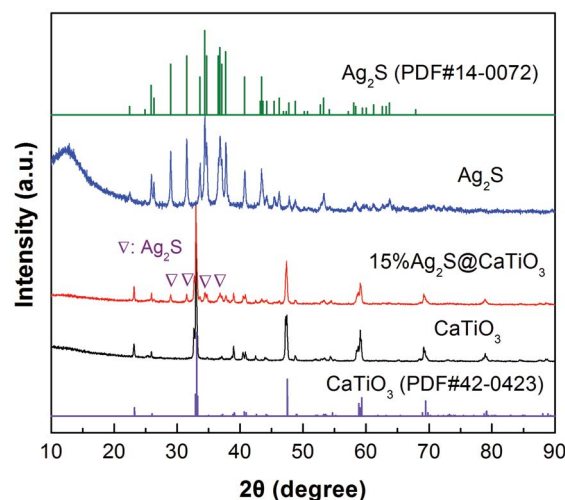


Fig. 1. XRD patterns of Ag_2S , CaTiO_3 and $15\%\text{Ag}_2\text{S}@/\text{CaTiO}_3$.

(PDF#14-0072, space group P21/n) and CaTiO_3 orthorhombic structure (JDF#42-0423, space group Pnma), respectively. For the $15\%\text{Ag}_2\text{S}@/\text{CaTiO}_3$ composite, besides the dominant diffraction peaks corresponding to CaTiO_3 , additional weak peaks assignable to Ag_2S are also observed on its XRD pattern. This indicates the integration of Ag_2S with CaTiO_3 . In addition, no other impurity phases are detected in the composite, implying that no chemical reaction between Ag_2S and CaTiO_3 occurs in the composite and their crystal structures undergo no change.

The microstructural morphologies of Ag_2S , CaTiO_3 and $15\%\text{Ag}_2\text{S}@/\text{CaTiO}_3$ were observed from SEM images. As seen from Figs. 2a and b, Ag_2S is crystallized into fine spherical nanoparticles with size of 7–17 nm (i.e., Ag_2S QDs). Due to their ultrafine size and high surface energy, these Ag_2S QDs are agglomerated into large-sized aggregate particles with size from several tens to a few hundreds of nanometers. The SEM images depicted in Figs. 2c and d demonstrate the formation of regular CaTiO_3 NCs with size of 0.8–1.1 μm in length and 0.3–0.5 μm in width. The surface of the CaTiO_3 NCs appears to be very clean and smooth. Figs. 2e and f display the SEM images of the $15\%\text{Ag}_2\text{S}@/\text{CaTiO}_3$ composite, from which one can see that Ag_2S QDs are uniformly assembled on the surface of CaTiO_3 NCs. No agglomeration behavior is observed for the Ag_2S QDs.

The microstructure of the $15\%\text{Ag}_2\text{S}@/\text{CaTiO}_3$ composite was further elucidated by TEM investigation. As displayed in Figs. 3a and b, the morphologies and sizes of Ag_2S QDs and CaTiO_3 NCs revealed by the TEM images are in perfect accordance with the SEM observation results. More importantly, the TEM images clearly demonstrate the uniform assembly of Ag_2S QDs on the surface of CaTiO_3 NCs. The chemical composition of the composite is determined by the EDS spectrum, as shown in Fig. 3c. It is seen that the elements of Ca, Ti, O, Ag and S are included in the composite. The atomic ratio between the heavy elements Ag, Ca and Ti suggests that the mass fraction of Ag_2S in the composite is basically in agreement with the stoichiometric composition of the $15\%\text{Ag}_2\text{S}@/\text{CaTiO}_3$ composite. However, the derived O content is lower than that in the CaTiO_3 phase, which

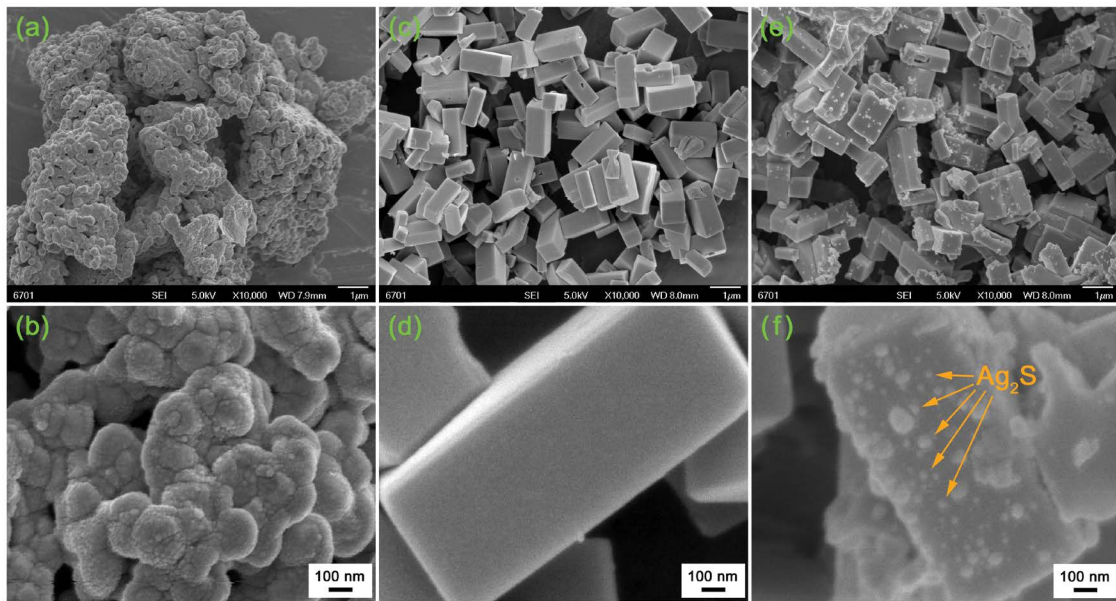


Fig. 2. SEM images of (a,b) Ag₂S QDs, (c,d) CaTiO₃ NCs and (e,f) the 15%Ag₂S@CaTiO₃ composite.

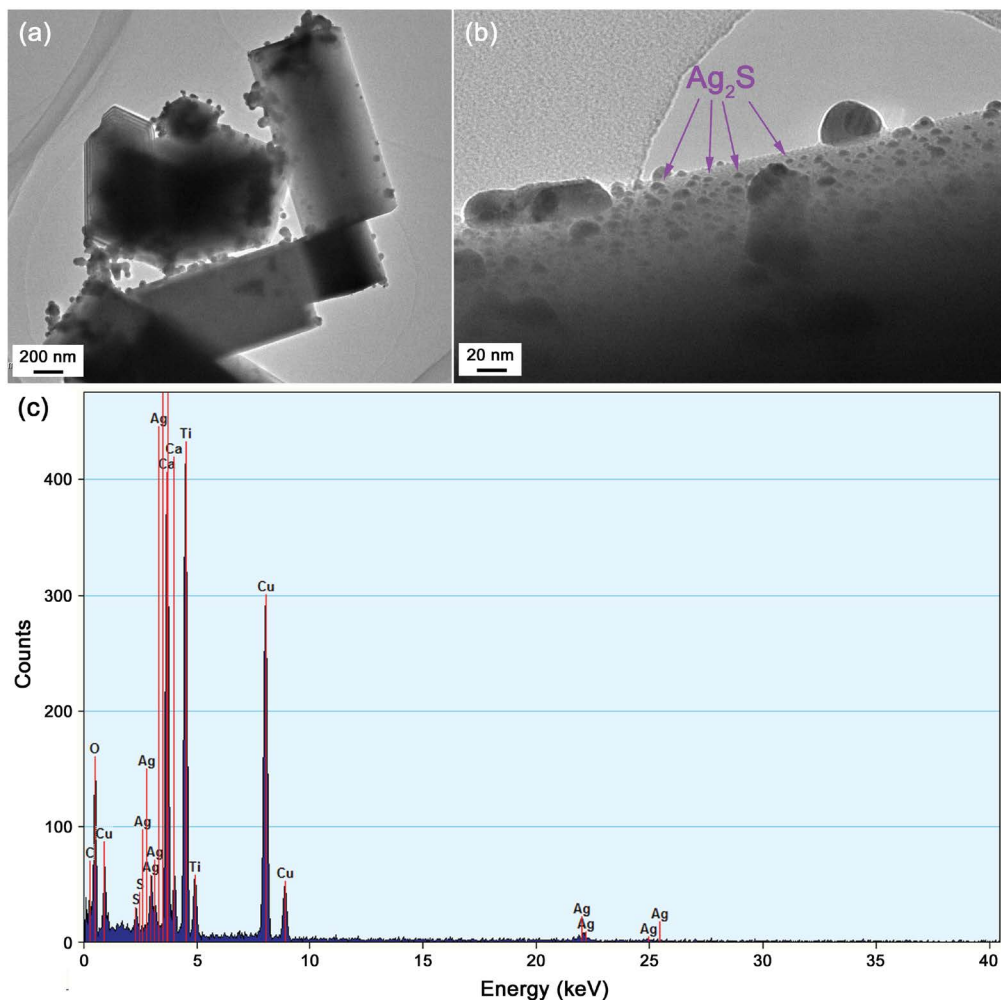


Fig. 3. TEM images (a,b) and EDS spectrum (c) of the 15%Ag₂S@CaTiO₃ composite.

could be ascribed to the non-sensitivity of EDS to light elements [61]. In addition, the observed Cu and C signals on the EDS spectrum could come from the TEM microgrid holder [62].

The elemental distribution of the 15%Ag₂S@CaTiO₃ composite was analyzed by EDX elemental mapping technique. The dark-field scanning TEM (DF-STEM) image of the composite given in Fig. 4a illustrates that CaTiO₃ NCs are homogeneously decorated with fine Ag₂S QDs. The corresponding elemental mapping images, as shown in Fig. 4b, demonstrate that the NCs are composed of Ca, Ti and O, and moreover, Ag and S elements are also seen to be uniformly distributed throughout the NCs. The EDX elemental mapping further confirms the decoration of Ag₂S QDs on the surface of CaTiO₃ NCs.

It is noted that the properties of nanomaterials are highly dependent on their optical absorption properties [63–65]. UV-vis diffuse reflectance spectroscopy is an useful method to measure optical absorption properties of nanomaterials. Figs. 5a and b depict the UV-vis DRS spectra and their corresponding first derivative curves of the samples, respectively. It is observed that Ag₂S QDs show a strong light absorption in the entire wavelength region measured in this work (200–850 nm). As a result, when Ag₂S QDs are assembled onto CaTiO₃ NCs, the obtained Ag₂S@CaTiO₃ composites manifest enhanced visible-light absorption compared to bare CaTiO₃ NCs. With increasing the Ag₂S content, the visible-light absorption of the composites gradually increases, which is further confirmed by the gradual deepening of their apparent color, from cream white for bare CaTiO₃ to dark gray for 20%Ag₂S@CaTiO₃, as illustrated in Fig. 5c. Whereas for bare Ag₂S QDs, a black color is observed. Due to their enhanced visible-light absorption, the Ag₂S@CaTiO₃ composite photocatalysts are expected to utilize photons from sunlight more effectively. The peak on the first derivative curves of the UV-vis DRS spectra can be characterized as the absorption edge of CaTiO₃ [48]. According to the relationship $E_g = 1,240/\lambda_{\text{abs}}$ (E_g and λ_{abs} represent the bandgap and absorption edge wavelength of the semiconductor, respectively), the E_g of CaTiO₃ is separately obtained as 3.39 (CaTiO₃), 3.59 (5%Ag₂S@CaTiO₃), 3.61 (10%Ag₂S@CaTiO₃), 3.64 (15%Ag₂S@CaTiO₃), and 3.66 eV (20%Ag₂S@CaTiO₃). A possible reason for the slight increase in the bandgap

of CaTiO₃ could be ascribed to the interaction between Ag₂S and CaTiO₃.

XPS analyses were performed on 15%Ag₂S@CaTiO₃ to determine its chemical states and composition. Fig. 6a displays the survey XPS spectrum, confirming that the composite is composed of the elements of Ca, Ti, O, Ag and S. The detected C signal comes from adventitious carbon that is used for the calibration of the binding energy scale (C 1s binding energy: 284.8 eV). The high-resolution XPS spectra of Ca 2p, Ti 2p, O 1s, Ag 3d and S 2p core levels are presented in Figs. 6b–f, respectively. On the Ca 2p XPS spectrum (Fig. 6b), the Ca 2p_{3/2} and Ca 2p_{1/2} core-electron binding energies are observed at 347.2 and 350.7 eV, respectively, implying that Ca species exists in the form of Ca²⁺ [48]. As shown in Fig. 6c, the Ti 2p XPS spectrum presents two peaks at 459.2 (Ti 2p_{3/2}) and 464.9 eV (Ti 2p_{1/2}) without detection of additional Ti 2p peaks, which implies that the Ti species behaves as Ti⁴⁺ oxidation state [48,66]. Two peaks are observed on the O 1s XPS spectrum (Fig. 6d), where the peak at 530.4 eV is assigned to the CaTiO₃ crystal lattice oxygen and the peak at 532.3 eV is contributed by chemisorbed oxygen species [48,67]. On the Ag 3d XPS spectrum (Fig. 6e), the observation of two sharp peaks at 368.3 (Ag 3d_{5/2}) and 374.3 eV (Ag 3d_{3/2}) is indicative of the presence of Ag⁺ oxidation state [68]. No additional peaks assignable to the metallic state of Ag are detected on the Ag 3d XPS spectrum. The S 2p XPS spectrum of (Fig. 6f) can be divided into two peaks at 161.2 and 162.4 eV, which correspond to S 2p_{3/2} and S 2p_{1/2}, respectively [68].

The possible existence of functional groups in CaTiO₃ and 15%Ag₂S@CaTiO₃ was examined by FTIR measurement, as shown in Fig. 7. The crystallization of CaTiO₃ perovskite-type structure is confirmed by the Ti–O–Ti bridging stretching mode resulting in the absorption peak at 560 cm⁻¹ [69]. The observed peaks at 1,403 (O–H in-plane deformation vibration of alcohols) and 1,105 cm⁻¹ (C–OH stretching vibration of alcohols) suggest that alcohols could be anchored on the samples during the washing process [37]. The broad absorption band in the range of 3,000–3,600 cm⁻¹ is caused by the N–H stretching vibration (3,146 cm⁻¹) and H–O stretching vibration (3,430 cm⁻¹). The absorption peak at 1,642 cm⁻¹ is induced by the H–O bending vibration. This implies water molecules and NH³⁺

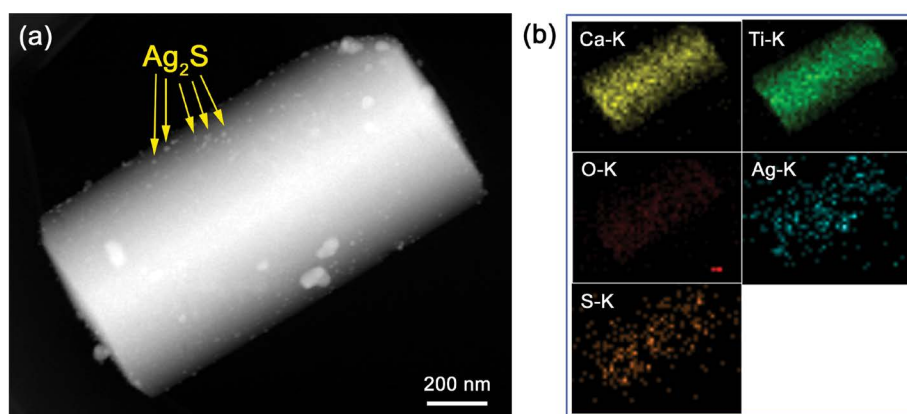


Fig. 4. DF-STEM image (a) and EDX elemental mapping images and (b) of the 15%Ag₂S@CaTiO₃ composite.

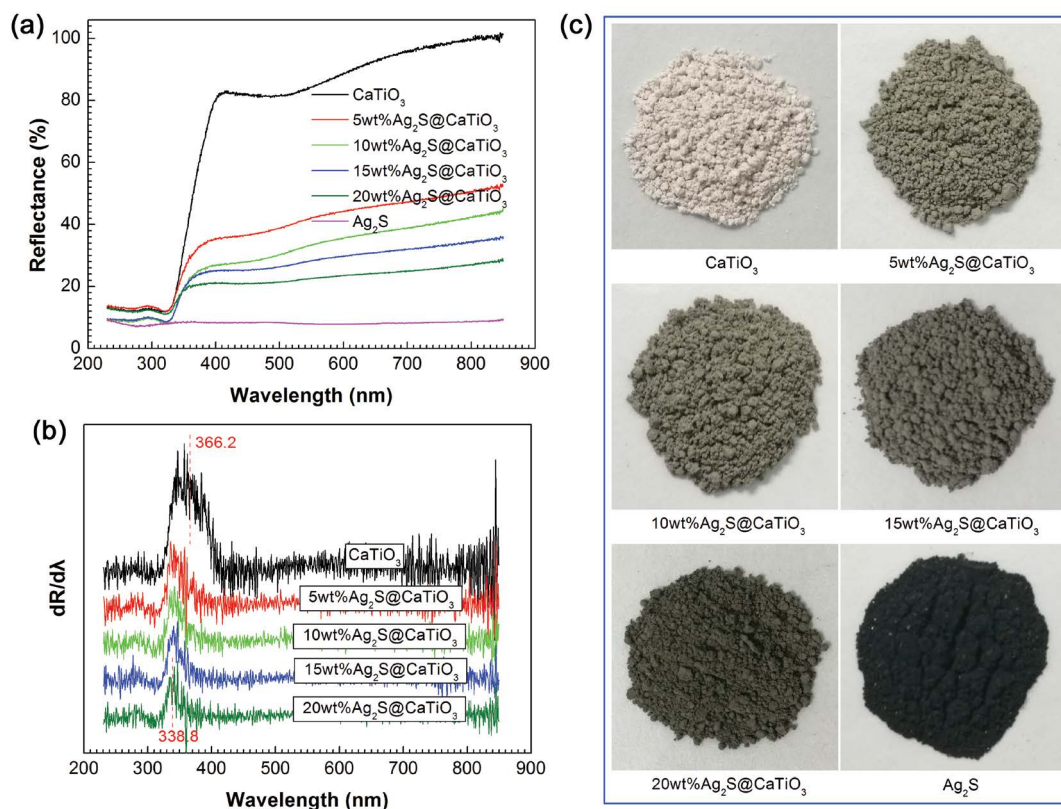


Fig. 5. UV-vis DRS spectra (a), first derivative curves of the UV-vis DRS spectra (b) and digital images (c) of CaTiO₃, Ag₂S and the 15%Ag₂S@CaTiO₃ composites.

groups are absorbed on the surface of the samples [70,71]. In addition, the 15%Ag₂S@CaTiO₃ composite shows no obvious characteristic peaks of Ag₂S QDs, which could be due to the low content and/or infrared inactivity of Ag₂S QDs.

PL spectroscopy is an useful technique to assess the recombination behavior of photogenerated e⁻/h⁺ pairs in semiconductor photocatalysts [72]. As shown in Fig. 8, an obvious PL emission peak at 555.4 nm, which arises due to the e⁻/h⁺ pair recombination, is observed for both CaTiO₃ and 15%Ag₂S@CaTiO₃. However, the 15%Ag₂S@CaTiO₃ composite manifests a relatively weak PL emission peak, indicating a decreased e⁻/h⁺ recombination in the composite.

Based on the photocurrent response and EIS analyses, We also compared the separation/transfer behavior of photoexcited carriers between CaTiO₃ and 15%Ag₂S@CaTiO₃. Fig. 9a shows the transient photocurrent-time curves of CaTiO₃ and 15%Ag₂S@CaTiO₃ under intermittent UV irradiation. An obvious photocurrent response behavior is observed for both the samples, and more importantly, the 15%Ag₂S@CaTiO₃ composite exhibits a higher photocurrent density than bare CaTiO₃ on the irradiation. As seen from Fig. 9b, the EIS spectra (Nyquist plots) of CaTiO₃ and 15%Ag₂S@CaTiO₃ display a typical semicircle shape. The observed smaller semicircle diameter for the composite implies that it has a relatively smaller charge-transfer resistance [73,74]. Based on the photocurrent response and EIS analyses, it is confirmed that the 15%Ag₂S@CaTiO₃ composite manifests a higher e⁻/h⁺ separation and faster interface charge transfer than bare CaTiO₃.

Separately under UV ($\lambda = 254$ nm) and visible light ($\lambda > 400$ nm) irradiation, the photocatalytic degradation performances of CaTiO₃ NCs, Ag₂S QDs and Ag₂S@CaTiO₃ composites were assessed by the elimination of RhB in aqueous solution. Before photocatalysis, the adsorption of RhB onto the samples was examined in the dark, and is obtained to be 3.5%–11.6%. The samples exhibit an increasing adsorption toward RhB with increasing the Ag₂S content. Generally, an appropriate dye adsorption is beneficial for its photocatalytic degradation. Fig. 10a illustrates the UV photocatalytic degradation of RhB over the samples, from which one can see that the Ag₂S@CaTiO₃ composites show a photocatalytic activity obviously higher than that of bare CaTiO₃ and Ag₂S. Among the composites, 15%Ag₂S@CaTiO₃ with a Ag₂S mass fraction of 15% manifests the highest photocatalytic activity. However, the decoration of excessive Ag₂S QDs on the surface of CaTiO₃ NCs is detrimental to the photocatalytic activity of resultant composites (e.g. 20%Ag₂S@CaTiO₃), which is due to the fact that excessive Ag₂S QDs could shield CaTiO₃ from light absorption. After photoreaction for 120 min, the degradation percentage of RhB is 79.2% for bare CaTiO₃ NCs and 65.4% for bare Ag₂S QDs, whereas the optimal composite sample 15%Ag₂S@CaTiO₃ photocatalyzes 99.6% removal of RhB. The photocatalytic activities between the samples are further compared by the kinetic analysis, as illustrated in Fig. 10b. The good linear relationship between $\ln(C_t/C_0)$ and irradiation time t implies that the dye degradation conforms to the pseudo-first-order kinetics described by $\ln(C_t/C_0) = -k_{app}t$ [75]. The apparent first-order reaction rate constant k_{app} is

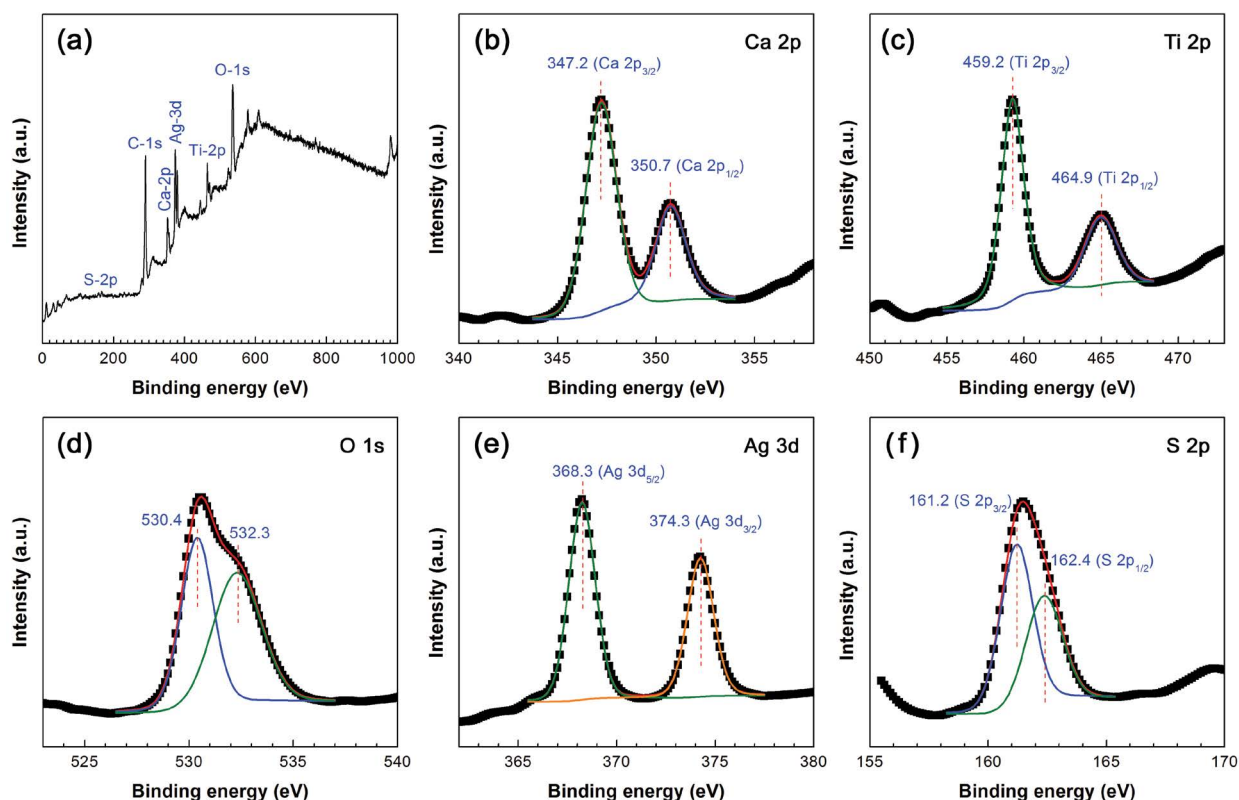


Fig. 6. Survey XPS spectrum (a) and high-resolution XPS spectra of (b) Ca 2p, (c) Ti 2p, (d) O 1s, (e) Ag 3d and (f) S 2p of the 15%Ag₂S@CaTiO₃ composite.

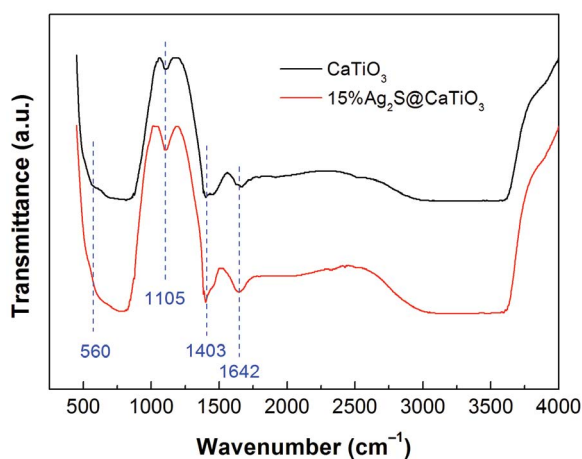


Fig. 7. FTIR spectra of CaTiO₃ and the 15%Ag₂S@CaTiO₃ composite.

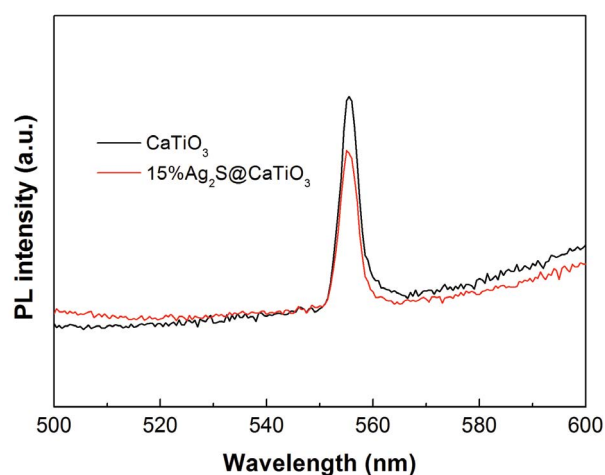


Fig. 8. PL spectra of CaTiO₃ and the 15%Ag₂S@CaTiO₃ composite.

obtained according to the linear-regression fitting, as inserted in Fig. 10b. From the reaction rate constants, it is confirmed that the photocatalytic activity of 15%Ag₂S@CaTiO₃ is about 3.6 and 5.6 times larger than that of bare CaTiO₃ NCs and Ag₂S QDs, respectively. The time-dependent UV-vis spectra of the RhB solution photocatalyzed by 15%Ag₂S@CaTiO₃ (Fig. S1) further confirms the photodegradation of RhB under UV irradiation. Fig. 10c shows the visible-light photocatalytic degradation of RhB over the samples. It is seen that CaTiO₃ is

nearly inactive under visible light irradiation, whereas Ag₂S shows an obvious visible light degradation activity. When Ag₂S QDs are assembled on the surface of CaTiO₃ NCs, the resultant Ag₂S@CaTiO₃ composites display an enhanced visible-light photocatalytic degradation of RhB compared to bare CaTiO₃ NCs, and their activity increases monotonically with increasing the Ag₂S content. The kinetic plots further confirm the visible-light photocatalytic performances of the samples, as shown in Fig. 10d.

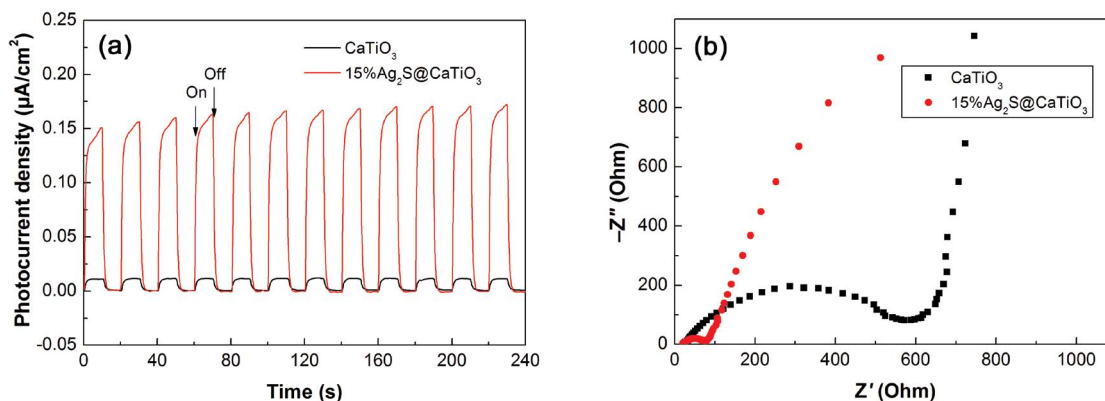


Fig. 9. Transient photocurrent response curves (a) and EIS spectra (b) of CaTiO_3 and the $15\%\text{Ag}_2\text{S}@CaTiO_3$ composite.

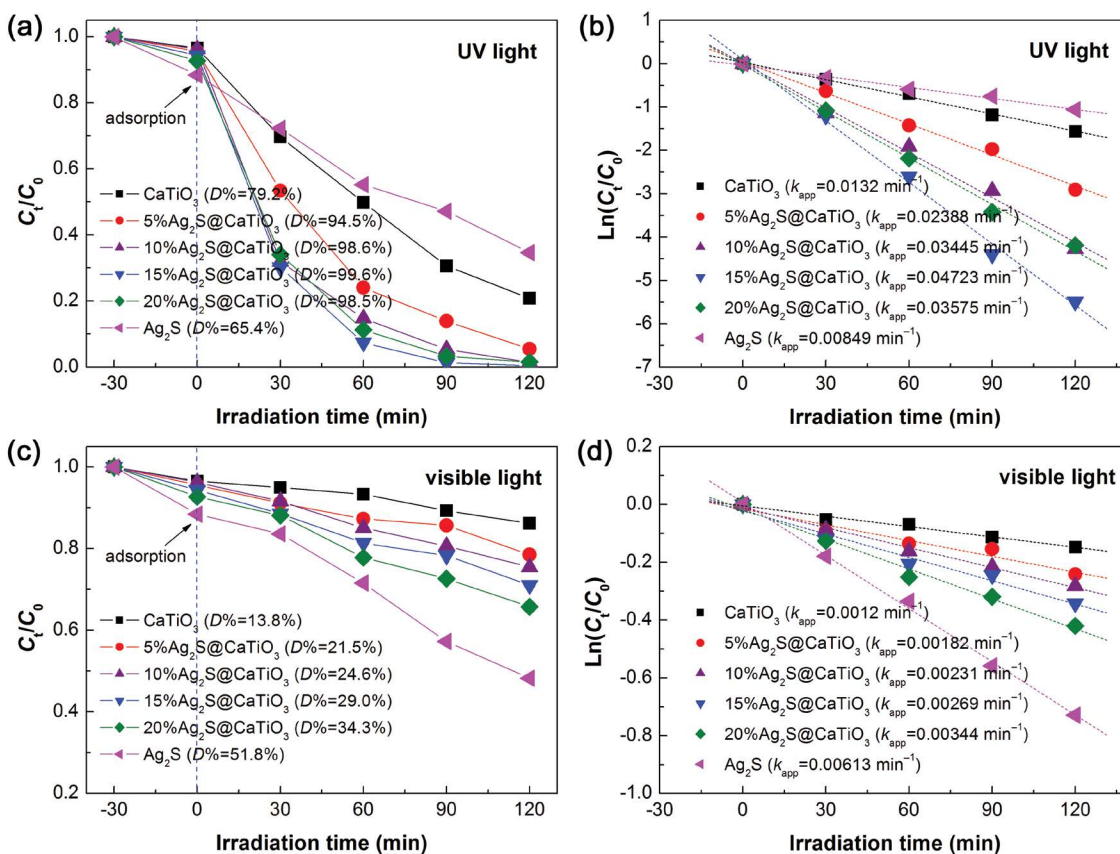


Fig. 10. (a) UV photocatalytic degradation of RhB over CaTiO_3 , Ag_2S and the $15\%\text{Ag}_2\text{S}@CaTiO_3$ composites. (b) Kinetic plots of the dye degradation over the samples under UV irradiation. (c) Visible-light photocatalytic degradation of RhB over the samples. (d) Kinetic plots of the dye degradation over the samples under visible light irradiation.

To elucidate the photocatalytic mechanism of the $\text{Ag}_2\text{S}@CaTiO_3$ composites, the CB and VB potentials of CaTiO_3 NCs were determined by the Mott-Schottky measurement according to the method described in the literature [76,77]. Fig. 11a shows the Mott-Schottky plots measured at 3,000 and 5,000 Hz, both of which yield a similar flat band potential (V_{FB}) of -1.08 V vs. SCE by extrapolating their linear portion to the x -axis. The SCE potential can be converted to the normal hydrogen electrode (NHE) potential according to

the relationship: $V(\text{NHE}) = V(\text{SCE}) + 0.059\text{pH} + 0.242$ (here $\text{pH} = 7$) [77]. CaTiO_3 behaves as an n -type semiconductor due to the positive slope of the Mott-Schottky plots. For an n -type semiconductor, the CB edge potential is assumed to be approximately equal to the flat band potential. Thus, the CB and VB potentials of CaTiO_3 NCs are estimated as -0.43 and $+2.96\text{ V}$ vs NHE ($E_g = 3.39\text{ eV}$).

Fig. 11b schematically shows the $\text{Ag}_2\text{S}@CaTiO_3$ heterostructures with Ag_2S QDs assembled on the surface of

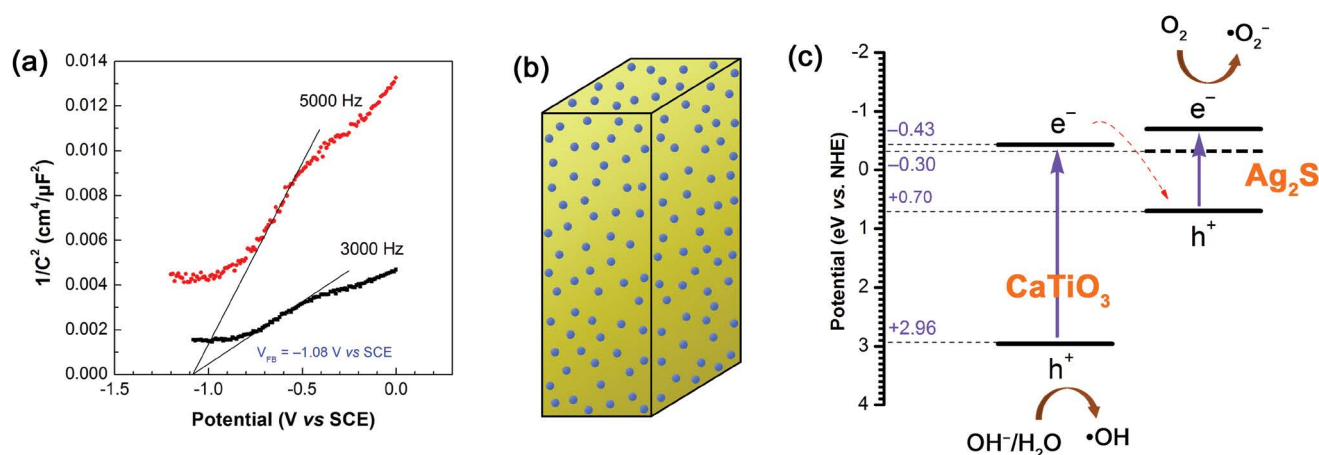


Fig. 11. (a) Mott–Schottky plots of CaTiO_3 measured at 3,000 and 5,000 Hz. (b) Schematic illustration of the $\text{Ag}_2\text{S}@CaTiO_3$ heterostructure composites. (c) Schematic illustration of the electron transfer and photocatalytic mechanism of the $\text{Ag}_2\text{S}@CaTiO_3$ composites.

CaTiO_3 NCs, and Fig. 11c schematically depicts the energy band diagrams of CaTiO_3 and Ag_2S . According to the literature, Ag_2S has a bandgap $E_g = 1.0$ eV and its CB and VB potentials are located at -0.30 and $+0.70$ V vs. NHE, respectively [61]. However, for tiny Ag_2S QDs, the quantum effect could induce a negative shift of their CB potential and increase of their bandgap [78]. As a result, CaTiO_3 and Ag_2S are expected to be coupled together to form Z-scheme $\text{Ag}_2\text{S}@CaTiO_3$ heterostructures due to their staggered band structure configuration, as shown in Fig. 11c. Under UV irradiation, both CaTiO_3 and Ag_2S are excited to generate electron/hole pairs. The CB electrons of CaTiO_3 will transfer to Ag_2S and recombine with its VB holes. This Z-scheme electron transfer and recombination process prolongs the lifetime of the VB holes in CaTiO_3 and CB electrons in Ag_2S , thus making them increasingly available for the photocatalytic reactions. This is the dominant reason for the enhanced photocatalytic performances of the $\text{Ag}_2\text{S}@CaTiO_3$ composites. Moreover, the coupling of Ag_2S QDs with CaTiO_3 NCs obviously enhances the visible light absorption and thus can make the best use of the solar energy to trigger the photocatalytic reactions.

To unveil the role of the reactive species—photoexcited h^+ , hydroxyl ($\cdot\text{OH}$) and superoxide ($\cdot\text{O}_2^-$) on the photodegradation of the dye, reactive species trapping experiments were carried out (Fig. S2). It is demonstrated that all these reactive species play an important role in the degradation of RhB. The role of the photoexcited h^+ is to react with OH^- or H_2O to produce the strong oxidant $\cdot\text{OH}$, instead of directly oxidizing the dye. This reaction process is ready to be proceeded since CaTiO_3 has a sufficiently positive VB potential of $+2.96$ V vs. NHE ($E^0(\text{H}_2\text{O}/\cdot\text{OH}) = +2.38$ vs. NHE, $E^0(\text{OH}^-/\cdot\text{OH}) = +1.99$ vs. NHE) [79]. $\cdot\text{O}_2^-$ can be easily produced through the reaction between the CB electron of Ag_2S with adsorbed O_2 owing to the sufficiently negative CB potential of Ag_2S (more negative than -0.3 V vs. NHE) compared to the redox potential of $\text{O}_2/\cdot\text{O}_2^-$ (-0.13 V vs. NHE) [79]. In addition, recycling photocatalytic experiment (Fig. S3) indicates that the $\text{Ag}_2\text{S}@CaTiO_3$ composite photocatalysts exhibit a good reusability for the photodegradation of the dye.

4. Conclusions

$\text{Ag}_2\text{S}@CaTiO_3$ hybrid composite photocatalysts were prepared by assembling Ag_2S QDs on the surface of CaTiO_3 NCs. Due to the Z-scheme electron transfer from the CB of CaTiO_3 to the VB of Ag_2S , the $\text{Ag}_2\text{S}@CaTiO_3$ composites exhibit highly efficient separation of photoexcited electron/hole pairs. As a result, more photoexcited holes in the VB of CaTiO_3 and electrons in the CB of Ag_2S are able to take part in the photodegradation reactions. Photocatalytic experiments confirm that the $\text{Ag}_2\text{S}@CaTiO_3$ composites manifest enhanced photocatalytic removal of RhB from aqueous solution under UV irradiation. In particular, the optimal composite sample 15% $\text{Ag}_2\text{S}@CaTiO_3$ can photocatalyze 99.6% removal of the dye after 120 min of UV irradiation, and it has a photocatalytic activity 3.6 and 5.6 times larger than that of bare CaTiO_3 NCs and Ag_2S QDs, respectively. Moreover, the decoration of Ag_2S QDs onto CaTiO_3 NCs can also enhance the visible-light photocatalytic degradation of the dye, implying that the $\text{Ag}_2\text{S}@CaTiO_3$ composites can efficiently use solar energy to drive the photocatalytic reactions.

Acknowledgements

This work was supported by the National Natural Science Foundation of China (Grant No. 51662027).

References

- [1] A.R. Khataee, M.B. Kasiri, Photocatalytic degradation of organic dyes in the presence of nanostructured titanium dioxide: influence of the chemical structure of dyes, *J. Mol. Catal. A: Chem.*, 328 (2010) 8–26.
- [2] N. Zhang, C. Han, X.Z. Fu, Y.-J. Xu, Function-oriented engineering of metal-based nanohybrids for photoredox catalysis: exerting plasmonic effect and beyond, *Chem*, 4 (2018) 1832–1861.
- [3] S.Q. Liu, Z.-R. Tang, Y.G. Sun, J.C. Colmenares, Y.-J. Xu, One-dimension-based spatially ordered architectures for solar energy conversion, *Chem. Soc. Rev.*, 44 (2015) 5053–5075.
- [4] B. Weng, M.-Y. Qi, C. Han, Z.-R. Tang, Y.-J. Xu, Photocorrosion inhibition of semiconductor-based photocatalysts: basic principle,

- current development, and future perspective, *ACS Catal.*, 9 (2019) 4642–4687.
- [5] L.J. Di, H. Yang, T. Xian, X.J. Chen, Facile synthesis and enhanced visible-light photocatalytic activity of novel $p\text{-Ag}_3\text{PO}_4/n\text{-BiFeO}_3$ heterostructure composites for dye degradation, *Nanoscale Res. Lett.*, 13 (2018) 257.
 - [6] W.H. Zhao, Z.Q. Wei, L. Zhang, X.J. Wu, X. Wang, Cr doped SnS_2 nanoflowers: preparation, characterization and photocatalytic decolorization, *Mater. Sci. Semicond. Process.*, 88 (2018) 173–180.
 - [7] Z.M. He, Y.M. Xia, B. Tang, J.B. Su, Fabrication and photocatalytic property of magnetic $\text{NiFe}_2\text{O}_4/\text{Cu}_2\text{O}$ composites, *Mater. Res. Express*, 4 (2017) 095501.
 - [8] J.P. Guin, D.B. Naik, Y.K. Bhardwaj, L. Varshney, An insight into the effective advanced oxidation process for treatment of simulated textile dye waste water, *RSC Adv.*, 4 (2014) 39941–39947.
 - [9] S.Y. Wang, H. Yang, Z. Yi, X.X. Wang, Enhanced photocatalytic performance by hybridization of Bi_2WO_6 nanoparticles with honeycomb-like porous carbon skeleton, *J. Environ. Manage.*, 248 (2019) 109341.
 - [10] Y.M. Xia, Z.M. He, K.J. Hu, B. Tang, J.B. Su, Y. Liu, X.P. Li, Fabrication of $n\text{-SrTiO}_3/p\text{-Cu}_2\text{O}$ heterojunction composites with enhanced photocatalytic performance, *J. Alloys Compd.*, 753 (2018) 356–363.
 - [11] P.V.L. Reddy, B. Kavitha, P.A.K. Reddy, K.H. Kim, TiO_2 -based photocatalytic disinfection of microbes in aqueous media: a review, *Environ. Res.*, 154 (2017) 296–303.
 - [12] Y.X. Yan, H. Yang, Z. Yi, T. Xian, NaBH_4 -reduction induced evolution of Bi nanoparticles from BiOCl nanoplates and construction of promising Bi@BiOCl hybrid photocatalysts, *Catalysts*, 9 (2019) 795.
 - [13] U. Alam, A. Khan, W. Raza, A. Khan, D. Bahnemann, M. Muneer, Highly efficient Y and V co-doped ZnO photocatalyst with enhanced dye sensitized visible light photocatalytic activity, *Catal. Today*, 284 (2017) 169–178.
 - [14] B. Weng, K.Q. Lu, Z.C. Tang, H.M. Chen, Y.J. Xu, Stabilizing ultrasmall Au clusters for enhanced photoredox catalysis, *Nat. Commun.*, 9 (2018) 1543.
 - [15] C.X. Zheng, H. Yang, Z.M. Cui, H.M. Zhang, X.X. Wang, A novel $\text{Bi}_4\text{Ti}_3\text{O}_{12}/\text{Ag}_3\text{PO}_4$ heterojunction photocatalyst with enhanced photocatalytic performance, *Nanoscale Res. Lett.*, 12 (2017) 608.
 - [16] Y.M. Xia, Z.M. He, J.B. Su, B. Tang, K.J. Hu, Y.L. Lu, S.P. Sun, X.P. Li, Fabrication of magnetically separable $\text{NiFe}_2\text{O}_4/\text{BiOI}$ nanocomposites with enhanced photocatalytic performance under visible-light irradiation, *RSC Adv.*, 8 (2018) 4284–4294.
 - [17] S.F. Wang, H.J. Gao, Y. Wei, Y.W. Li, X.H. Yang, L.M. Fang, L. Lei, Insight into the optical, color, photoluminescence properties, and photocatalytic activity of the N-O and C-O functional groups decorating spinel type magnesium aluminate, *CrystEngComm*, 21 (2019) 263–277.
 - [18] S. Ghosh, S. Basu, M. Baskey, Decorating mechanism of Mn_2O_3 nanoparticles on reduced graphene oxide surface through reflux condensation method to improve photocatalytic performance, *J. Mater. Sci. - Mater. Electron.*, 28 (2017) 17860–17870.
 - [19] S.Y. Wang, H. Yang, X.X. Wang, W.J. Feng, Surface disorder engineering of flake-like Bi_2WO_6 crystals for enhanced photocatalytic activity, *J. Electron. Mater.*, 48 (2019) 2067–2076.
 - [20] X.X. Wang, J.K. Zhu, H. Tong, X.D. Yang, X.X. Wu, Z.Y. Pang, H. Yang, Y.P. Qi, A theoretical study of a plasmonic sensor comprising a gold nano-disk array on gold film with an SiO_2 spacer, *Chin. Phys. B*, 28 (2019) 044201.
 - [21] X.X. Wang, J.K. Zhu, X.L. Wen, X.X. Wu, Y. Wu, Y.W. Su, H. Tong, Y.P. Qi, H. Yang, Wide range refractive index sensor based on a coupled structure of Au nanocubes and Au film, *Opt. Mater. Express*, 9 (2019) 3079–3088.
 - [22] K.A.S. Fernando, S.P. Sahu, Y. Liu, W.K. Lewis, E. Gulianti, A. Jafariyan, P. Wang, C.E. Bunker, Y.P. Sun, Carbon quantum dots and applications in photocatalytic energy conversion, *ACS Appl. Mater. Interfaces*, 7 (2015) 8363–8376.
 - [23] P. Devil, A. Thakur, S.K. Bhardwaj, S. Saini, P. Rajput, P. Kumar, Metal ion sensing and light activated antimicrobial activity of Aloe vera derived carbon dots, *J. Mater. Sci. - Mater. Electron.*, 29 (2018) 17254–17261.
 - [24] X.X. Wang, X.L. Bai, Z.Y. Pang, J.K. Zhu, Y. Wu, H. Yang, Y.P. Qi, X.L. Wen, Surface-enhanced Raman scattering by composite structure of gold nanocube-PMMA-gold film, *Opt. Mater. Express*, 9 (2019) 1872–1881.
 - [25] J.L. Jiang, X.X. He, J.F. Du, X.J. Pang, H. Yang, Z.Q. Wei, In-situ fabrication of graphene-nickel matrix composites, *Mater. Lett.*, 220 (2018) 178–181.
 - [26] Z. Yi, J. Huang, C.L. Cen, X.F. Chen, Z.G. Zhou, Y.J. Tang, B.Y. Wang, Y.G. Yi, J. Wang, P.H. Wu, Nanoribbon-ring cross perfect metamaterial graphene multi-band absorber in THz range and the sensing application, *Results Phys.*, 14 (2019) 102367.
 - [27] J. Huang, G. Niu, Z. Yi, X.F. Chen, Z.G. Zhou, X. Ye, Y.J. Tang, T. Duan, Y. Yi, Y.G. Yi, High sensitivity refractive index sensing with good angle and polarization tolerance using elliptical nanodisk graphene metamaterials, *Phys. Scr.*, 94 (2019) 085805.
 - [28] Y.B. Zhang, C.L. Cen, C.P. Liang, Z. Yi, X.F. Chen, M.W. Li, Z.G. Zhou, Y.J. Tang, Y.G. Yi, G.F. Zhang, Dual-band switchable terahertz metamaterial absorber based on metal nanostructure, *Results Phys.*, 14 (2019) 102422.
 - [29] C.L. Cen, Y.B. Zhang, C.P. Liang, X.F. Chen, Z. Yi, T. Duan, Y.J. Tang, X. Ye, Y.G. Yi, S.Y. Xiao, Numerical investigation of a tunable metamaterial perfect absorber consisting of two-intersecting graphene nanoring arrays, *Phys. Lett. A*, 383 (2019) 3030–3035.
 - [30] X.X. Wang, Z.Y. Pang, H. Yang, Y.P. Qi, Theoretical study of subwavelength circular grating fabrication based on continuously exposed surface plasmon interference lithography, *Results Phys.*, 14 (2019) 102446.
 - [31] S.I. Sadovnikov, E.G. Vovkotrub, Thermal stability of nanoparticle size and phase composition of nanostructured Ag_2S silver sulfide, *J. Alloys Compd.*, 766 (2018) 140–148.
 - [32] L.J. Di, H. Yang, T. Xian, X.J. Chen, Construction of Z-scheme $\text{g-C}_3\text{N}_4/\text{CNT}/\text{Bi}_2\text{Fe}_4\text{O}_9$ composites with improved simulated-sunlight photocatalytic activity for the dye degradation, *Micromachines*, 9 (2018) 613.
 - [33] N. Zhang, M.Q. Yang, S.Q. Liu, Y.G. Sun, Y.J. Xu, Waltzing with the versatile platform of graphene to synthesize composite photocatalysts, *Chem. Rev.*, 115 (2015) 10307–10377.
 - [34] K.Q. Lu, X. Xin, N. Zhang, Z.R. Tang, Y.J. Xu, Photoredox catalysis over graphene aerogel-supported composites, *J. Mater. Chem. A*, 6 (2018) 4590–4604.
 - [35] M.-L. Yang, N. Zhang, K.-Q. Lu, Y.-J. Xu, Insight into the role of size modulation on tuning the band gap and photocatalytic performance of semiconducting nitrogen-doped graphene, *Langmuir*, 33 (2017) 3161–3169.
 - [36] P. She, K.L. Xu, S. Zeng, Q.R. He, H. Sun, Z.N. Liu, Investigating the size effect of Au nanospheres on the photocatalytic activity of Au-modified ZnO nanorods, *J. Colloid Interface Sci.*, 499 (2017) 76–82.
 - [37] S. Khanchandani, P.K. Srivastava, S. Kumar, S. Ghosh, A.K. Ganguli, Band gap engineering of ZnO using core/shell morphology with environmentally benign Ag_2S sensitizer for efficient light harvesting and enhanced visible-light photocatalysis, *Inorg. Chem.*, 53 (2014) 8902–8912.
 - [38] H.J. Gao, C.X. Zheng, H. Yang, X.W. Niu, S.F. Wang, Construction of a $\text{CQDs}/\text{Ag}_3\text{PO}_4/\text{BiPO}_4$ heterostructure photocatalyst with enhanced photocatalytic degradation of rhodamine B under simulated solar irradiation, *Micromachines*, 10 (2019) 557.
 - [39] W. Jiang, Z.M. Wu, X.N. Yue, S.J. Yuan, H.F. Lu, B. Liang, Photocatalytic performance of Ag_2S under irradiation with visible and near-infrared light and its mechanism of degradation, *RSC Adv.*, 5 (2015) 24064–24071.
 - [40] H. Abdullah, D.H. Kuo, Facile synthesis of n-type $(\text{AgIn})_x\text{Zn}_{2(1-x)}\text{S}_2/p\text{-type Ag}_2\text{S}$ nanocomposite for visible light photocatalytic reduction to detoxify hexavalent chromium, *ACS Appl. Mater. Interfaces*, 7 (2015) 26941–26951.
 - [41] L.J. Di, T. Xian, X.F. Sun, H.Q. Li, Y.J. Zhou, J. Ma, H. Yang, Facile preparation of $\text{CNT}/\text{Ag}_2\text{S}$ nanocomposites with improved visible and NIR light photocatalytic degradation activity and their catalytic mechanism, *Micromachines*, 10 (2019) 503.
 - [42] B. Barrocas, T.J. Entradas, C.D. Nunes, O.C. Monteiro, Titanate nanofibers sensitized with ZnS and Ag_2S nanoparticles as novel photocatalysts for phenol removal, *Appl. Catal., B*, 218 (2017) 709–720.

- [43] H. Li, F. Xie, W. Li, H. Yang, R. Snyders, M.F. Chen, W.J. Li, Preparation and photocatalytic activity of $\text{Ag}_2\text{S}/\text{ZnS}$ core-shell composites, *Catal. Surv. Asia*, 22 (2018) 156–165.
- [44] M.D. Biegalski, L. Qiao, Y. Gu, A. Mehta, Q. He, Y. Takamura, A. Borisevich, L.Q. Chen, Impact of symmetry on the ferroelectric properties of CaTiO_3 thin films, *Appl. Phys. Lett.*, 106 (2015) 162904.
- [45] S. Tariq, A. Ahmed, S. Saad, S. Tariq, Structural, electronic and elastic properties of the cubic CaTiO_3 under pressure: a DFT study, *AIP Adv.*, 5 (2015) 77111.
- [46] B.G. Park, Photoluminescence of Eu^{3+} -doped CaTiO_3 perovskites and their photocatalytic properties with a metal ion loading, *Chem. Phys. Lett.*, 722 (2019) 44–49.
- [47] X. Yan, X.J. Huang, Y. Fang, Y.H. Min, Z.J. Wu, W.S. Li, J.M. Yuan, L.G. Tan, Synthesis of rodlike CaTiO_3 with enhanced charge separation efficiency and high photocatalytic activity, *Int. J. Electrochem. Sci.*, 9 (2014) 5155–5163.
- [48] Y.X. Yan, H. Yang, Z. Yi, T. Xian, X.X. Wang, Direct Z-scheme $\text{CaTiO}_3/\text{BiOBr}$ composite photocatalysts with enhanced photodegradation of dyes, *Environ. Sci. Pollut. Res.*, (2019), <https://doi.org/10.1007/s11356-019-06085-y>.
- [49] S.N. Lim, S.A. Song, Y.C. Jeong, H.W. Kang, S.B. Park, K.Y. Kim, H_2 production under visible light irradiation from aqueous methanol solution on CaTiO_3/Cu prepared by spray pyrolysis, *J. Electron. Mater.*, 46 (2017) 6096–6103.
- [50] W.X. Dong, B. Song, G.L. Zhao, W.J. Meng, G.R. Han, Effects of the volume ratio of water and ethanol on morphosynthesis and photocatalytic activity of CaTiO_3 by a solvothermal process, *Appl. Phys. A*, 123 (2017) 348.
- [51] T. Alammar, I. Hamma, M. Warkb, A.V. Mudring, Low-temperature route to metal titanate perovskite nanoparticles for photocatalytic applications, *Appl. Catal., B*, 178 (2015) 20–28.
- [52] T. Kimijima, K. Kanie, M. Nakaya, A. Muramatsu, Hydrothermal synthesis of size- and shape-controlled CaTiO_3 fine particles and their photocatalytic activity, *CrystEngComm*, 16 (2014) 5591–5597.
- [53] M. Ye, M. Wang, D. Zheng, N. Zhang, C. Lin, Z. Lin, Garden-like perovskite superstructures with enhanced photocatalytic activity, *Nanoscale*, 6 (2014) 3576–3584.
- [54] Y.X. Yan, H. Yang, Z. Yi, R.S. Li, X.X. Wang, Enhanced photocatalytic performance and mechanism of Au/CaTiO_3 composites with Au nanoparticles assembled on CaTiO_3 nanocuboids, *Micromachines*, 10 (2019) 254.
- [55] A. Alzahrani, D. Barbash, A. Samokhvalov, “One-pot” synthesis and photocatalytic hydrogen generation with nanocrystalline $\text{Ag}(0)/\text{CaTiO}_3$ and in situ mechanistic studies, *J. Phys. Chem. C*, 120 (2016) 19970–19979.
- [56] L.M. Lozano-Sanchez, S. Obregon, L.A. Diaz-Torres, S.W. Lee, V. Rodriguez-Gonzalez, Visible and near-infrared light-driven photocatalytic activity of erbium-doped CaTiO_3 system, *J. Mol. Catal. A: Chem.*, 410 (2015) 19–25.
- [57] L.Y. Bai, Q. Xu, Z.S. Cai, Synthesis of $\text{Ag}/\text{AgBr}/\text{CaTiO}_3$ composite photocatalyst with enhanced visible light photocatalytic activity, *J. Mater. Sci. - Mater. Electron.*, 29 (2018) 17580–17590.
- [58] F.R. Cesconeto, M. Borlaf, M.I. Nieto, A.P.N. de Oliveira, R. Moreno, Synthesis of CaTiO_3 and $\text{CaTiO}_3/\text{TiO}_2$ nanoparticle compounds through $\text{Ca}^{2+}/\text{TiO}_2$ colloidal sols: structural and photocatalytic characterization, *Ceram. Int.*, 44 (2018) 301–309.
- [59] X.B. Ning, S.S. Ge, X.T. Wang, H. Li, X.R. Li, X.Q. Liu, Y.L. Huang, Preparation and photocathodic protection property of $\text{Ag}_2\text{S}-\text{TiO}_2$ composites, *J. Environ. Chem. Eng.*, 6 (2018) 311–324.
- [60] X.X. Zhao, H. Yang, Z.M. Cui, Z. Yi, H. Yu, Synergistically enhanced photocatalytic performance of $\text{Bi}_4\text{Ti}_3\text{O}_{12}$ nanosheets by Au and Ag nanoparticles, *J. Mater. Sci. - Mater. Electron.*, 30 (2019) 13785–13796.
- [61] Z.M. He, Y.M. Xia, J.B. Su, B. Tang, Fabrication of magnetically separable $\text{NiFe}_2\text{O}_4/\text{Bi}_4\text{Ti}_3\text{O}_{12}$ nanocomposites and excellent photocatalytic performance under visible light irradiation, *Opt. Mater.*, 88 (2019) 195–203.
- [62] Y.C. Ye, H. Yang, H.M. Zhang, J.L. Jiang, A promising $\text{Ag}_2\text{CrO}_4/\text{LaFeO}_3$ heterojunction photocatalyst applied to photo-Fenton degradation of RhB, *Environ. Technol.*, (2018), <https://doi.org/10.1080/09593330.2018.1538261>.
- [63] C.L. Cen, Z. Yi, G.F. Zhang, Y.B. Zhang, C.P. Liang, X.F. Chen, Y.J. Tang, X. Ye, Y.G. Yi, J.Q. Wang, J.J. Hua, Theoretical design of a triple-band perfect metamaterial absorber in the THz frequency range, *Results Phys.*, 14 (2019) 102463.
- [64] Y.B. Zhang, C.L. Cen, C.P. Liang, Z. Yi, X.F. Chen, Y.J. Tang, T. Yi, Y.G. Yi, W. Luo, S.Y. Xiao, Five-band terahertz perfect absorber based on metal layer-coupled dielectric metamaterial, *Plasmonics*, (2019), <https://doi.org/10.1007/s11468-019-00956-3>.
- [65] H. Tong, Y.Q. Xu, Y.W. Su, X.X. Wang, Theoretical study for fabricating elliptical subwavelength nanohole arrays by higher-order waveguide-mode interference, *Results Phys.*, 14 (2019) 102460.
- [66] Y.M. Xia, Z.M. He, Y.L. Lu, B. Tang, S.P. Sun, J.B. Su, X.P. Li, Fabrication and photocatalytic property of magnetic $\text{SrTiO}_3/\text{NiFe}_2\text{O}_4$ heterojunction nanocomposites, *RSC Adv.*, 8 (2018) 5441–5450.
- [67] M. Pooladi, H. Shokrollahi, S.A.N.H. Lavasani, H. Yang, Investigation of the structural, magnetic and dielectric properties of Mn-doped $\text{Bi}_2\text{Fe}_4\text{O}_{13}$ produced by reverse chemical co-precipitation, *Mater. Chem. Phys.*, 229 (2019) 39–48.
- [68] D.A. Reddy, R. Ma, M.Y. Choi, T.K. Kim, Reduced graphene oxide wrapped $\text{ZnS}-\text{Ag}_2\text{S}$ ternary composites synthesized via hydrothermal method: applications in photocatalyst degradation of organic pollutants, *Appl. Surf. Sci.*, 324 (2015) 725–735.
- [69] A.S. Roy, S.G. Hegde, A. Parveen, Synthesis, characterization, AC conductivity, and diode properties of polyaniline- CaTiO_3 composites, *Polym. Adv. Technol.*, 25 (2014) 130–135.
- [70] S.F. Wang, H.J. Gao, L.M. Fang, Y. Wei, Y.W. Li, L. Lei, Synthesis and characterization of BaAl_2O_4 catalyst and its photocatalytic activity towards degradation of methylene blue dye, *Z. Phys. Chem.*, 233 (2018), doi: <https://doi.org/10.1515/zpch-2018-1308>.
- [71] B.D. Mert, M.E. Mert, G. Kardas, B. Yazici, Experimental and theoretical studies on electrochemical synthesis of poly(3-amino-1,2,4-triazole), *Appl. Surf. Sci.*, 258 (2012) 9668–9674.
- [72] H.J. Gao, F. Wang, S.F. Wang, X.X. Wang, Z. Yi, H. Yang, Photocatalytic activity tuning in a novel $\text{Ag}_2\text{S}/\text{CQDs}/\text{CuBi}_2\text{O}_4$ composite: synthesis and photocatalytic mechanism, *Mater. Res. Bull.*, 115 (2019) 140–149.
- [73] X.L. Zhu, Z.Q. Wei, W.H. Zhao, X.D. Zhang, L. Zhang, X. Wang, Microstructure and electrochemical properties of ZnMn_2O_4 nanopowder synthesized using different surfactants, *J. Electron. Mater.*, 47 (2018) 6428–6436.
- [74] T.T. Bi, H.Q. Fang, J.L. Jiang, X.X. He, X. Zhen, H. Yang, Z.Q. Wei, Z.F. Jia, Enhance supercapacitive performance of $\text{MnO}_2/3\text{D}$ carbon nanotubes/graphene as a binder-free electrode, *J. Alloys Compd.*, 787 (2019) 759–766.
- [75] C.X. Zheng, H. Yang, Assembly of Ag_3PO_4 nanoparticles on rose flower-like Bi_2WO_6 hierarchical architectures for achieving high photocatalytic performance, *J. Mater. Sci. - Mater. Electron.*, 29 (2018) 9291–9300.
- [76] F. Cardon, W.P. Gomes, On the determination of the flat-band potential of a semiconductor in contact with a metal or an electrolyte from the Mott-Schottky plot, *J. Phys. D: Appl. Phys.*, 11 (1978) L63–L67.
- [77] X.X. Zhao, H. Yang, H.M. Zhang, Z.M. Cui, W.J. Feng, Surface-disorder-engineering-induced enhancement in the photocatalytic activity of $\text{Bi}_4\text{Ti}_3\text{O}_{12}$ nanosheets, *Desal. Wat. Treat.*, 145 (2019) 326–336.
- [78] R.P. Panmand, G. Kumar, S.M. Mahajan, M.V. Kulkarni, D.P. Amalnerkar, B.B. Kale, S.W. Gosavi, Functionality of bismuth sulfide quantum dots/wires-glass nanocomposite as an optical current sensor with enhanced Verdet constant, *J. Appl. Phys.*, 109 (2011) 033101.
- [79] L.J. Di, H. Yang, T. Xian, X.Q. Liu, X.J. Chen, Photocatalytic and photo-Fenton catalytic degradation activities of Z-scheme $\text{Ag}_2\text{S}/\text{BiFeO}_3$ heterojunction composites under visible-light irradiation, *Nanomaterials*, 9 (2019) 399.

Supplementary information

UV-vis spectra of the RhB solution photocatalyzed by 15%Ag₂S@CaTiO₃ at different times under UV irradiation were measured using U-2001 UV-vis spectrophotometer, as shown in Fig. S1. It is seen that the intensity of the characteristic absorption peaks of RhB decreases with increasing the reaction time, confirming the degradation of RhB during the photocatalytic process.

Hydroxyl ($\cdot\text{OH}$), superoxide ($\cdot\text{O}_2^-$) and photoexcited h^+ are generally considered to be the main active species in most of photocatalytic systems. To elucidate their role in the RhB degradation over 15%Ag₂S@CaTiO₃, reactive species trapping experiments were carried out by using ethanol as the scavenger of $\cdot\text{OH}$, benzoquinone (BQ) as the scavenger of $\cdot\text{O}_2^-$ and ammonium oxalate (AO) as the scavenger of photoexcited h^+ . An amount of ethanol (5 mL), BQ (0.1 mmol) and AO (0.1 mmol) were separately added in the reaction solution (100 mL of 5 mg L⁻¹ RhB solution +0.1 g of 15%Ag₂S@CaTiO₃). The adsorption and photocatalytic degradation experiments were performed under the procedure same to that without adding scavengers. UV light was used the light source. As illustrated in Fig. S2, all the scavengers have an important suppression on the photodegradation of RhB, implying that $\cdot\text{OH}$, $\cdot\text{O}_2^-$ and h^+ plays an important role in the photodegradation reactions.

Recycling photocatalytic experiment was carried out to assess the reusability of the 15%Ag₂S@CaTiO₃ composite photocatalyst toward the degradation of RhB under UV irradiation. After the completion of each photodegradation

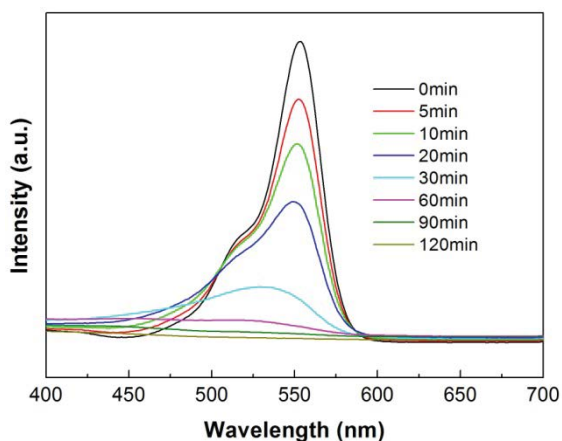


Fig. S1. UV-vis absorption spectra of RhB solution photocatalyzed by 15%Ag₂S@CaTiO₃.

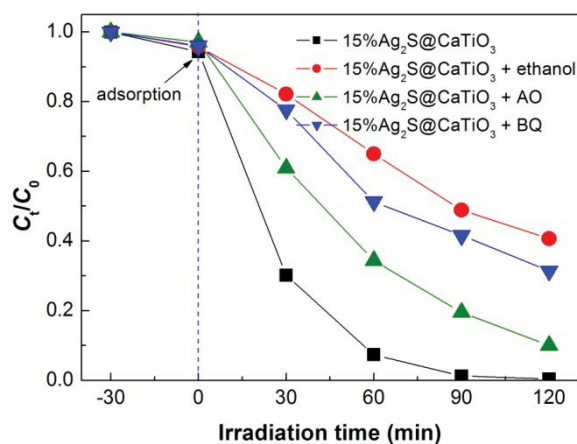


Fig. S2. Effect of ethanol, BQ and AO on the degradation of RhB over 15%Ag₂S@CaTiO₃ under UV irradiation.

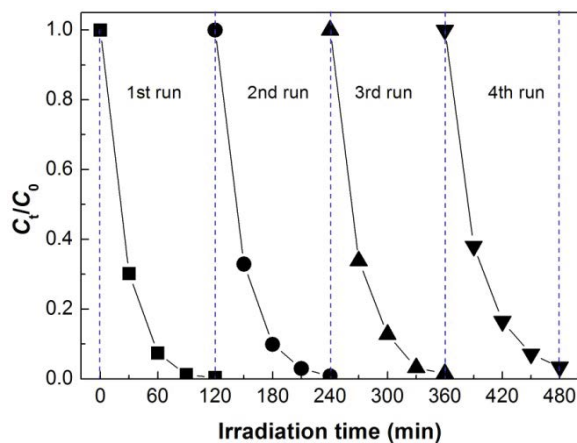


Fig. S3. Reusability of 15%Ag₂S@CaTiO₃ for the photodegradation of RhB under UV irradiation.

cycle, the sample was collected and recovered by washing with deionized water and drying at 60°C for 5 h. The recovered sample was added in 100 mL of fresh RhB solution and then irradiated for the next photocatalytic cycle. As seen from Fig. S3, the 15%Ag₂S@CaTiO₃ composite still shows a high photocatalytic removal of RhB at the 4th photocatalytic cycle, indicative of a good recycling stability of the composite photocatalyst.